Interferometric experiments on the transmission matrix of diffusive neutral inclusions

ANDREAS NIEMEYER,[1,5] PAUL SCHROFF,[2] WONJUN CHOI,[3] JAECHEOL CHO,[3] ANDREAS NABER,[1] WONSHIK CHOI,[3] AND MARTIN WEGENER[1,4,6]

[1]*Institute of Applied Physics, Karlsruhe Institute of Technology, 76128 Karlsruhe, Germany*
[2]*Department of Physics, SUPA, University of Strathclyde, Glasgow G4 0NG, United Kingdom*
[3]*IBS Center for Molecular Spectroscopy and Dynamics Department of Physics, Korea University, South Korea*
[4]*Institute of Nanotechnology, Karlsruhe Institute of Technology, 76128 Karlsruhe, Germany*
[5]*Andreas.Niemeyer@kit.edu*
[6]*Martin.Wegener@kit.edu*

Abstract: By using tailored disorder in the regime of diffusive light propagation, core-shell cloaking structures have previously been presented. These structures make the cloak and an arbitrary interior nearly indistinguishable from the diffusive surrounding. This statement holds true for all incident polarizations of light, a broad range of incident directions of light in three dimensions, and a broad range of visible wavelengths. Here, by performing interferometric transmission-matrix experiments, we investigate the statistical wave properties of miniaturized versions of such structures. By using singular-value decomposition, we derive the eigenchannels and eigenvalues to assess the degree of wave correlation among multiply scattered waves. We find small but significant differences in the eigenvalue distributions, suggesting that the degree of wave correlation is lower for the neutral inclusion than for a homogeneously disordered reference sample, which corresponds to the surrounding of the neutral inclusion. Likewise, we find similar differences between optically inspecting the core-shell neutral-inclusion and its spatial neighborhood. These differences allow us to reveal the neutral inclusion due to different statistics of the underlying random walks of light.

1. Personal foreword

In his scientific oeuvre, Costas Soukoulis made significant contributions to the fields of disordered or complex optical systems [1] and optical metamaterials [2]. Here, we present a set of recent original experimental results on the transmission matrix of diffusive optical neutral inclusions on the occasion of Costas Soukoulis' 70th birthday. On a small spatial scale, these structures are composed of randomly distributed nanoparticles, the density of which is arranged in a core-shell manner on a larger spatial scale. The cylindrical core-shell geometry can be seen as one wound-up unit cell of an anisotropic laminate metamaterial. Therefore, these experiments relate to both of the above fields to which Costas Soukoulis has made pioneering contributions.

2. Introduction

The mathematics and physics of diffusive-optical core-shell cloaks [3] are analogous to that of magneto-static cloaks [4] and thermal cloaks under stationary conditions [5] (see Fig. 1(a)). It goes back to the 1956 work of Kerner [6], has been described several times in the literature [4–7] including a dedicated review article [8]. In brief, an inner strongly light-scattering cylinder (the core) with outer radius R_1 isolates the core's interior from its exterior.

This is a peer-reviewed, accepted author manuscript of the following article: Niemeyer, A., Schroff, P., Choi, W., Cho, J., Naber, A., Choi, W., & Wegener, M. (2021). Interferometric experiments on the transmission matrix of diffusive neutral inclusions. Journal of the Optical Society of America B, 38(9), C42-C49. https://doi.org/10.1364/JOSAB.425847

Ideally, the light diffusivity of this inner cylinder is zero, $D_1 = 0$. A cylindrical shell with inner radius R_1, outer radius R_2, and light diffusivity $D_2 = D_0(R_2^2 + R_1^2)/(R_2^2 - R_1^2)$ around this core molds the diffusive flow of light around the core such that the emerging light becomes indistinguishable from that of the homogeneous disordered surrounding of the cloak with diffusivity D_0. Within the range of validity of the diffusion equation, this statement is strictly true for spatially homogeneous stationary illumination [3,8]. Under these conditions, for negligibly small optical absorption and identical scattering particles of concentrations n_0 in the surrounding and n_2 in the shell, respectively, we further have the relation $D_2/D_0 = (n_2/n_0)^{-1}$. This relation holds true because the optical diffusivity is proportional to the optical transport mean free path length [9], and the transport mean free path length is inversely proportional to the concentration of scattering particles.

The core and the shell can be seen as one period of a laminate metamaterial [10]. For spatially inhomogeneous stationary illumination, such a diffusive cloak works only approximately but still quite well [8]. Improved cloaking can, in principle, be achieved by using multiple laminate periods instead of just a single period for the core-shell geometry. However, the price to be paid is very low overall optical transmission [11] compared to the core-shell arrangement. Therefore, we only consider diffusive core-shell structures in this paper. Precisely, due to fabrication restrictions, we do not drill an inner hole into the diffusive core (the core's outer radius is already as small as $R_1 = 0.8$ mm), thus the absence of this hole conceptually turns the core-shell invisibility cloak into a core-shell invisible object or neutral inclusion.

It would be interesting to further improve the above-mentioned diffusive architectures. Here, we follow a different path and rather explore the underlying fundamental limitations.

In the case of diffusive core-shell cloaks, it is instructive to think about the propagating light waves in terms of light rays or, loosely speaking, as point-like photons. Photons impinging onto the core are guided around the core within the surrounding shell. The shell exhibits a larger light diffusivity $D_2 > D_0$ than the surrounding medium, D_0. The larger light diffusivity corresponds to a larger mean free path length. Therefore, photons traveling through the shell and emerging from the sample have accumulated a shorter overall average path length than photons travelling through the homogeneous surrounding. Furthermore, the path length distributions and their widths are different, too. However, the relative thickness of the shell, R_2/R_1, is designed such that the transmission probabilities are the same. This design ensures that the transmittance is the same and that the core and its interior become invisible.

Due to the different path length distributions, time-of-flight measurements could differentiate between the cloak and the homogeneously disordered reference sample [12]. These experiments showed that photons arrive earlier and the time-of-flight distribution is narrower for the cloak case than for the reference. This finding suggests that the core-shell cloak is effectively a less-scattering medium than the diffusive surrounding. Calculations of the photon statistics analyzed by Monte-Carlo simulations indeed showed that the number of photon scattering events is smaller for the cloak than for the reference.

Another possibility to reveal or uncloak the cloak is to measure the degree of multiple light scattering by speckle experiments [13]. In these experiments using a variable finite coherence length of light, it was found that the cloak exhibited a larger speckle interference contrast than the reference sample. This difference was most pronounced if the coherence length of light roughly matched the width of the path length distribution. These experimental findings were well reproduced by theory.

A third approach for distinguishing between the invisible object and a homogeneous diffusive surrounding is based on measuring the associated transmission matrices. In the ideal case, the transmission matrix contains all information on light waves transmitting through the complex disordered scattering medium [14]. This includes the information on the average path length as well as on the width of the path length distribution. Transmission-matrix experiments have been performed for homogeneously disordered specimen [15–18].

Furthermore, random-matrix theory can be applied for the case of homogeneously disordered systems [19]. However, much less is known about inhomogeneously disordered media in three dimensions, with one notable exception [20]. There, the eigenvalue distribution of the transmission matrix, which is a good measure of the correlation between different partial waves [21], was determined. Long-range correlations among multiply scattered waves can lead to constructive interference. As a result, the maximum eigenvalue of the transmission matrix with respect to the mean eigenvalues increases [20]. In addition, larger long-range correlations increase the variance of the normalized eigenvalues of the transmission matrix [22].

In this paper, we measure the transmission matrices of a neutral inclusion sample and a homogeneously disordered reference sample. In these interferometric experiments, we find small but significant differences in the eigenvalue distributions of the transmission matrices. In order to perform these experiments, a new generation of samples has been designed and realized.

3. Optical samples

The samples used in our previous experiments [3,23] had two issues that prevented us from performing optical transmission-matrix experiments. First, the thickness of the samples was $L_z = 6$ cm [3] and $L_z = 3$ cm [23], respectively. In the setup to be used below, L_z needs to be smaller than the free working distance of the high-numerical-aperture microscope objective lenses (4 mm). Second, our previous samples were based on water [3] or a mechanically soft PDMS matrix [23]. For the water-based samples, we could not even observe speckle patterns due to the rapid Brownian motion of the nanoparticles. The PDMS-based samples exhibited speckle patterns that gradually changed over a timescale of about one minute. Therefore, a stationary optical transmission matrix did not exist for either case.

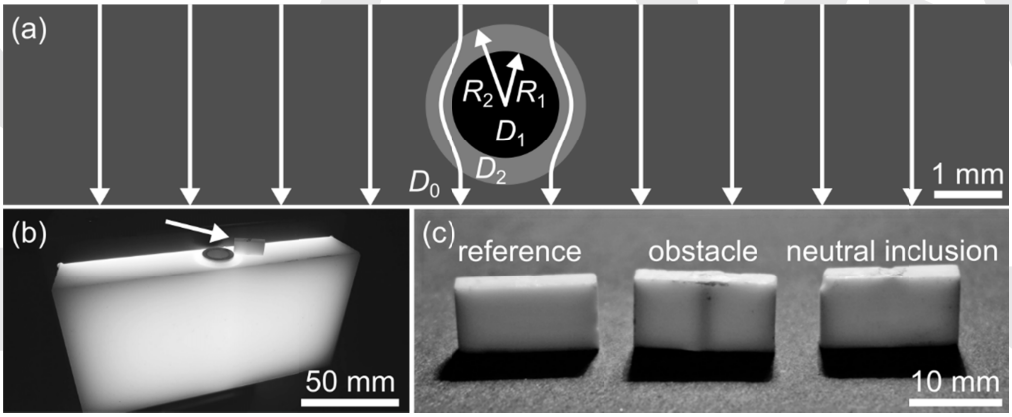

Fig. 1. (a) Illustration of a cylindrical diffusive-optical core-shell neutral-inclusion with radii R_1 and R_2 in an otherwise homogeneously disordered surrounding. The piece-wise constant light diffusivities D_0, D_1, and D_2 are indicated. (b) Comparison of the (large) invisibility-cloak sample used in our previous work [13,23] (using a hollow core rather than a solid core) and the (small) neutral-inclusion sample used in the present work (see white arrow). (c) Photographs of the samples discussed in the present work: Reference sample (left), obstacle sample (middle), and core-shell neutral-inclusion sample (right). The width of these cuboid samples is $L_x = 15$ mm, their height is $L_y = 8$ mm, and their thickness is $L_z = 3$ mm. Furthermore, we have $R_1 = 0.8$ mm and $R_2 = 1.2$ mm.

Here, we solve both issues by implementing two measures. First, we scale down all sample dimensions by an order of magnitude. To obtain the same optical properties, we need to scale down all mean free paths of light by an order of magnitude as well. This means that we need to increase the concentrations of scattering nanoparticles in all regions of the

structure by an order of magnitude. Second, we use mechanically stiff epoxy as a matrix (SKresin 2420 (TS) - S u. K Hock GmbH). The samples are fabricated by doping the epoxy with titania nanoparticles (DuPont R700 TiO2 particles, diameter ≈ 340 nm) at different densities. This composite is filled into mechanically machined aluminum molds, followed by thermal polymerization. Experimentally, we find the best performance for the concentration ratio $n_0/n_2 = 4.1$. In the surrounding, the absolute concentration, n_0, of nanoparticles in the epoxy corresponds to 3.9 mg/ml. For the core, in order to achieve as low as possible light diffusivity D_1, one would ideally want to use titania nanoparticles without any epoxy. However, this choice would not be stable mechanically. Therefore, we use a weight ratio of titania nanoparticles to epoxy of three to one, corresponding to 1,700 mg/ml.

In Fig. 1, the design of the core-shell neutral-inclusion sample (a), a size comparison between the larger old cloak [23] and the smaller new neutral inclusion (b), and a photograph of the three new samples (c) are shown.

White-light sample characterization experiments on these three samples along the lines of our previous work [3,23] are depicted in Fig. 2.

In agreement with earlier sample generations [3,23], the pronounced diffusive-optical shadow for the "obstacle" sample nearly disappears for the "neutral-inclusion" sample, making its behavior closely similar to that of the "reference" sample – both, for homogeneous illumination and point-like illumination of the sample front side (see Fig. 2). However, the invisibility performance of the miniaturized samples depicted in Fig. 2 is somewhat deteriorated with respect to our previous cloak samples [23]. These correspondingly contained an about ten times lower concentrations of titania nanoparticles.

In what follows, we only consider the core-shell neutral-inclusion and the reference sample because the obstacle sample can immediately be distinguished from the reference sample by the naked eye (cf. Fig.1(c)), making sophisticated experiments and an analysis of the obstacle sample in terms of transmission eigenvalues pointless.

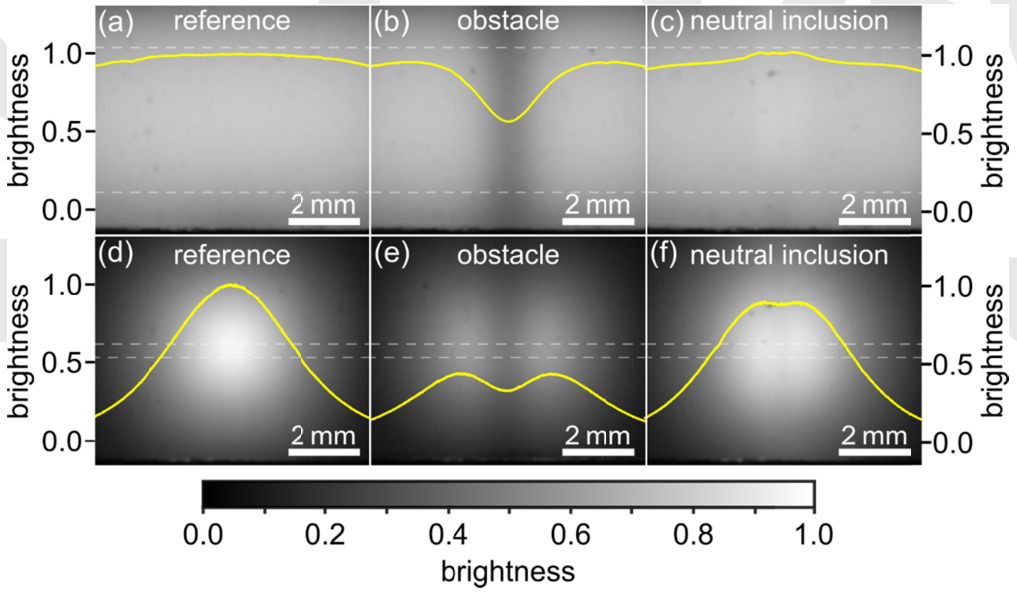

Fig. 2. Photographs of the transmitted light of the reference, obstacle, and neutral-inclusion samples used in this work (cf. Fig. 1(c)) under illumination with white light from the other side of the sample. The top row corresponds to homogeneous illumination of the sample front surface and the bottom row to point-like illumination. The yellow curves superimposed onto these photographs exhibit intensity cuts through these photographs, averaged over the range indicated by the dashed gray horizontal lines. For clarity, these cuts are normalized to the peak brightness value of the reference sample (a) for (a)-(c) and to that of (d) for (d)-(f), respectively.

4. Transmission-matrix experiments

The general approach of transmission-matrix experiments to be presented in this Section and the analysis based on singular-value decomposition in Section 5 are well known from the literature, but tend to be somewhat uneasy to digest at first sight. Therefore, we start with a basic introduction.

Let us consider a given and fixed frequency of light. The transmission matrix relates the transmitted light through a sample to the incident light. It is a subset of a scattering matrix which covers all the outgoing waves including reflected light. The input and output can, for example, be represented by the electric-vector field of the electromagnetic light wave. This complex-valued vector field contains information on the polarization, the amplitude, and the phase of light. Therefore, the elements of the transmission matrix are complex-valued as well. For both, input and output, the problem can be formulated in either real (r) space or wave-vector (k) space. This leaves one with four different possibilities for representing the transmission matrix: r-r, r-k, k-r, and k-k for input-output. Below, we will choose one possibility that is particularly well suited for our conditions. In principle, one should consider all, that is, infinitely many possible inputs and infinitely many possible outputs. In an experiment, only a finite number of inputs and outputs can be considered. Generally, the number of input possibilities and the number of output possibilities need not be identical, in which case the transmission matrix relating input and output is not a square matrix. For example, one may consider 100 different input wave vectors of light and characterize the output in real space by an image containing $30 \times 30 = 900$ pixels. The resulting transmission matrix is a 900×100 matrix, for which, mathematically, eigenvalues and eigenvectors do not exist. It may be desirable though to determine something like eigenvalues and eigenvectors. The corresponding mathematical procedure is known as singular-value decomposition [14,18,24] and will be summarized in Section 5 for our conditions using our nomenclature. In essence, this mathematical procedure is the generalization of a unitary transformation applied to a square matrix that leads to a diagonal matrix, the diagonal elements of which are the eigenvalues. The singular values are the mathematical generalization of eigenvalues. For our above example, one would have 100 singular values (rank of the matrix). The physical meaning of a singular value is the amplitude transmittance of an associated input eigenvector to the detection channels. The square modulus of the singular value is called an eigenvalue, and it corresponds to the intensity transmittance of the associated eigenvector. For example, if one considers the transmission matrix of a volume element of vacuum, all square moduli of the singular values are identical to unity. For a medium absorbing all the light, all square moduli would be zero. In our below analysis, we will additionally normalize the square moduli of the singular values to their mean value.

Let us now turn to our specific experiments. As discussed previously [8], point-like illumination of the cloak or neutral-inclusion region on the front side of the sample is a more demanding test for the invisibility performance than homogeneous illumination or non-centered spot illumination. Therefore, aiming at revealing the invisible object, we use a fixed position of a narrowly collimated beam waist on the sample front side, while varying the directions of the incident light. This means that the input to the transmission matrix is in wave-vector space. We emphasize that the choice of fixing the illuminated spot position may not be ideal when aiming at characterizing homogeneously disordered samples. This choice is, however, well suited for the spatially inhomogeneous cylindrical core-shell structures of interest here.

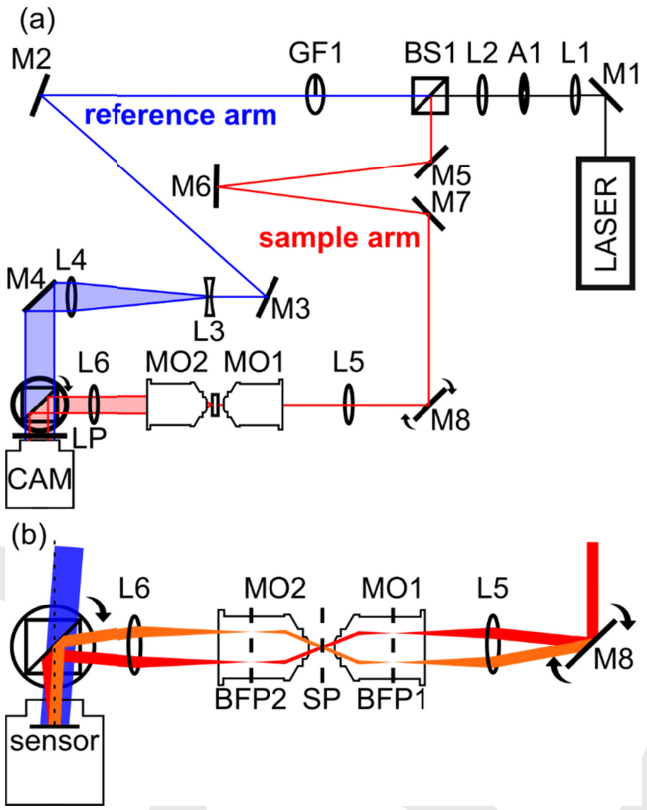

Fig. 3. Scheme of the optical transmission-matrix experiment. (a) Overview over the entire interferometer containing a sample arm (red) and a reference arm (blue). The focal lengths of the lenses are L1: 75 mm, L2: 50 mm, L3: −9 mm, L4: 200 mm, L5: 75 mm, L6: 100 mm. The distance between lenses of a pair is adjusted such that a collimated beam results. A1 is a 50 µm pinhole, M1-M7 are fixed Mirrors, M8 is a tunable micro-mirror. BS1 and BS2 are 50%/50% beam splitters and GF1 is a variable gray filter. MO1 and MO2 are microscope objective lenses and LP is a linear polarizer. (b) Magnified view onto the sample arm and the combination of sample and reference arm on the CCD camera. The reference beam and the optical axis intentionally include an angle $\gamma = 2.5°$, which is exaggerated in the drawing for clarity. This angle leads to a tilt in both the horizontal and vertical direction on the CCD camera chip (cf. dashed white circle in Fig. 4(b)). The MEMS mirror allows to vary the direction of the incident light while keeping the position of the illuminated spot on the front side of the sample fixed. We vary the angle by $\pm 23°$ in both directions with a spacing between adjacent directions of 0.47° in both directions. This combination leads to 7,845 different and independent illumination configurations. This number defines the number of columns of the transmission matrix. The number of rows of the transmission matrix results from the choices discussed in Fig. 4 and is $(361)^2 = 130{,}321$.

Our setup for measuring the transmission matrix is illustrated in Fig. 3. We use a laser (Toptica, DL 100) operating at $\lambda = 780$ nm wavelength with a coherence length of > 1 m. A telescope formed by lens L5 and the microscope objective MO1 (Leitz Wetzlar, $\infty/0$, $50\times, \mathrm{NA} = 0.6$) de-magnifies the laser beam diameter to about $2r_1 = 200$ µm at the sample position. This size is smaller than the diameter, $2R_1 = 1.6$ mm, of the core of the core-shell structure. MO1 and L5 together form a $4f$ imaging system. When tilting the laser beam by using the tunable micro-mirror device M8, the laser focus is displaced in the back-focal plane BFP1. MO1 translates this displacement into a variation of the angle of incidence of the beam in the sample plane SP – while the position of the beam on the sample front side is fixed. We emphasize again that this aspect is not important for homogeneously disordered samples, but

it is crucial for intentionally spatially inhomogeneous samples, such as the core-shell structure. Here, unless explicitly stated otherwise, we position the laser spot on the center of the core-shell structure (cf. Fig. 1) as we expect that this configuration is the most sensitive test. This expectation is indeed fulfilled (see below). We estimate that the maximum number of independent gaussian plane waves that can be delivered through the area πr_1^2 via the objective lens with a numerical aperture of 0.6 is close to 300,000. Here, we acquire data for 7,845 different incident directions of light, which are arranged in a square array in angular space, truncated by a circle, corresponding to 75% of the numerical aperture. Conceptually, the sequence of measuring the different incident directions is not relevant. For convenience, we start from normal incidence of light and proceed towards increasingly oblique angles in a 2D spiral shape.

We have chosen the angular spread of the individual illumination configurations and the total number of illumination configurations such that we obtain a sufficiently large number of *independent* (i.e., non-overlapping) illumination configurations. This aspect is crucial. In an early stage of our experiments, we had chosen smaller numbers of independent illumination configurations. This choice did not allow us to distinguish between the core-shell structure and the reference sample (see below).

The light emerging from the sample is collected by a second microscope lens MO2, which is identical to the first one (MO1). MO2 together with lens L6 form another $4f$ imaging system. The light emerging from the sample is sent onto a silicon-based optical camera (Point Grey, BFLY-PGE-50H5M-C). Precisely, in the case of no sample, the setup images the sample plane (SP) onto the camera chip. This means that the output of the transmission matrix is in real space, while its input is in wave-vector space (see above). In case of measuring the reference or core-shell sample, we position the front surface of the sample in the sample plane (SP). Therefore, the input plane of the transmission matrix lies in SP. In order to avoid ambiguous realignments of the setup when switching between no sample and any of the samples, we leave the alignment of all optical components untouched and the same as in the case of no sample. As a result, the imaging path is somewhat distorted due to the additional optical path length introduced by the samples, which have a refractive index of about 1.5 and a physical thickness $L_z = 3\ \mathrm{mm}$. This means that we only approximately image the rear side of the samples onto the camera. The output of the transmission matrix therefore only approximately corresponds to real space.

On the camera chip, the light from the sample arm interferes pixel-wise with the expanded and collimated beam from the reference arm of the setup (cf. Fig. 4(a)). The reference arm is intentionally aligned such that it includes an angle of about 2.5 degrees with the light transmitted from the sample arm. This arrangement can be seen as off-axis holography between the sample and the reference beam. Thereby, after Fourier-transforming the 2D camera image, the interference term between the sample and the reference arm is well separated from the autocorrelations of the sample and the reference beams in Fourier space (see Fig. 4(b)). Due to the finite numerical aperture of the collecting microscope lens, the useful data lie within a circle. All pixels outside of that circle bounded by a circle with a diameter of 361 pixels are set to zero. Using an inverse fast Fourier transform, a 361×361 square array is transformed back to 361×361 pixels in 2D real space on the camera chip (see Fig. 4(c) and 4(d)). These data are complex-valued and contain the phase information of the light transmitted by the sample. For the mathematical treatment, these 2D images are arranged into a single vector with $361 \times 361 = 130{,}321$ elements.

To summarize this section, our transmission matrix, $\overleftrightarrow{T}$, connects 130,321 output points in real space to 7,845 input wave vectors or incident directions of light. This statement is strictly true for the case of no sample. With a sample in the sample arm, this statement is only true approximately. The numbers of input directions and real-space output points, respectively, are chosen as large as possible while appreciating memory, aperture, and pixilation constrains. Mathematically, the transmission matrix is composed of the complex-valued

elements T_{ij}. The index i runs over its 130,321 rows and the index j runs over its 7,845 columns, leading to $130{,}321 \times 7{,}845 = 1{,}022{,}368{,}245$ elements of the transmission matrix.

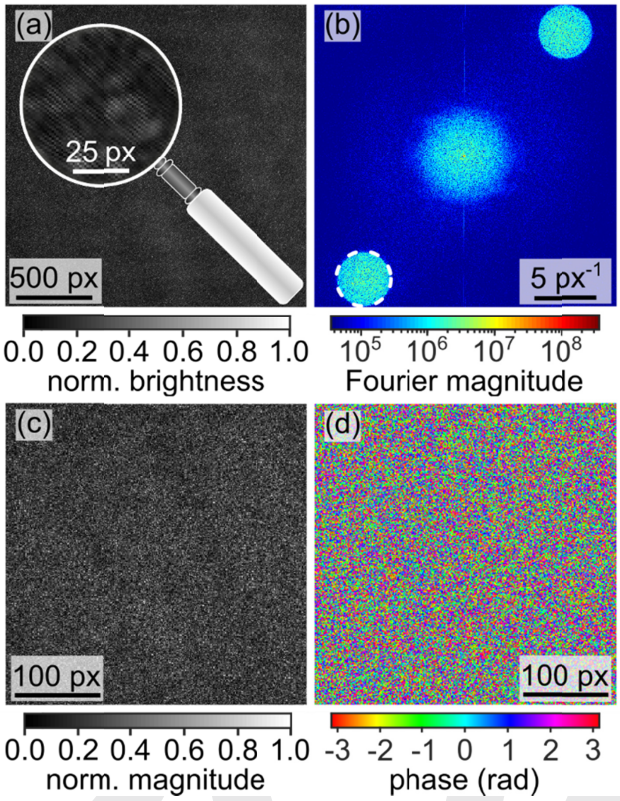

Fig. 4. (a) Example camera raw image, a speckle pattern, for one selected incident direction of light (cf. Fig. 3). Light from the sample arm and the reference arm (cf. Fig. 3) interfere on the camera pixels. The inset highlights the resulting interference stripes due to the angle $\gamma \neq 0$ and the fact that the speckle pattern is spatially resolved. The side length of one pixel on the camera chip corresponds to 0.1 µm in the sample plane (cf. SP in Fig. 3(b)). (b) Modulus of the Fourier transform of (a) on a logarithmic false-color scale. The contribution arising from the interference of the sample and reference arm is highlighted by the dashed white circle. All pixels outside of this white circle are set to zero, and the center of the white circle is chosen as the new coordinate origin (0,0) in momentum space. Inverse Fourier transformation of these data leads to panels (c) and (d). (c) Modulus and (d) phase. These two panels each contain $(361)^2 = 130{,}321$ pixels, which defines the numbers of rows of the transmission matrix (cf. caption of Fig. 3).

5. Singular value decomposition

To extract useful information from the measured optical transmission matrices $\vec{\vec{T}}$, we perform a singular value decomposition [14,18,24] according to

$$\vec{\vec{T}} = \vec{\vec{U}}\,\vec{\vec{\sigma}}\,\vec{\vec{V}}^{*}.$$

Here, $\vec{\vec{U}}$ is a $m \times m = 130{,}321 \times 130{,}321$ unitary matrix, $\vec{\vec{\sigma}}$ is a $m \times n = 130{,}321 \times 7{,}845$ matrix, $\vec{\vec{V}}^{*}$ is a $n \times n = 7{,}845 \times 7{,}845$ unitary matrix, and $\vec{\vec{V}}^{*}$ is the conjugate transpose of $\vec{\vec{V}}$. The upper $7{,}845 \times 7{,}845$ block of the matrix $\vec{\vec{\sigma}}$ (i.e., the elements σ_{ij} with row index $i = 1 \ldots 7{,}845$) is a diagonal matrix. Its diagonal elements σ_{ii} with $i = 1 \ldots 7{,}845$ lead to the transmission eigenvalues $|\sigma_{ii}|^2$ of the sample. These obey the relation

$$\sum_{i=1}^{n}|\sigma_{ii}|^2 = \sum_{i=1}^{m}\sum_{j=1}^{n}|T_{ij}|^2 .$$

We use the normalization

$$\sum_{i=1}^{n}|\sigma_{ii}|^2 = n.$$

The eigenvalues are ordered according to their square modulus, such that $|\sigma_{11}|^2 > |\sigma_{22}|^2 \ldots > |\sigma_{nn}|^2$. The lower part of the matrix $\overleftrightarrow{\sigma}$ (i.e., the elements σ_{ij} with row index $i = 7{,}846 \ldots 130{,}321$) contains zeroes only. Any j-th column of $\overleftrightarrow{U}$ (with $j = 1 \ldots 130{,}321$) obeys the normalization condition

$$\sum_{i=1}^{m}|U_{ij}|^2 = 1 ,$$

and the j-th row of $\overleftrightarrow{V}^*$ (with $j = 1 \ldots 7{,}845$) obeys the normalization

$$\sum_{j=1}^{n}|V_{ij}^*|^2 = 1 .$$

The columns of the unitary matrix $\overleftrightarrow{U}$ form an orthonormal basis. Hence, the columns can be interpreted as eigenmodes or eigenchannels, which refer to the output of the transmission matrix. For visualization, each of the $130{,}321$ columns can be arranged backwards (see above) into a 2D image with 361×361 pixels. The rows of the unitary matrix $\overleftrightarrow{V}^*$ form an orthonormal basis, which refers to the input of the transmission matrix. For visualization, each of the $7{,}845$ rows can likewise be arranged backwards (see above) into a 2D image.

We emphasize that the resulting distributions of the transmission eigenvalues versus index i are immune against the absolute average transmission of the samples, which strictly drops out in the described analysis due to the used normalization $\sum_{i=1}^{n}|\sigma_{ii}|^2 = n$. Therefore, different distributions of the transmission eigenvalues of different samples reflect different statistics of the underlying random walks of light in these samples.

6. Results and discussion

It is instructive to start our discussion with the case of no sample between the two microscope objective lenses. The experimental result is shown by the black curve in Fig. 5. It is clear that the transmission matrix of no sample is the same as the transmission matrix of free space. This means that, for all incident directions, the transmission should ideally be strictly equal to unity. From Fig. 5, we see that this is not the case. We rather find a monotonic decrease versus index i. The decrease itself results from the ordering described above. The fact that the eigenvalues are not all the same is due to experimental imperfections. It originates from the following factors. First, when approaching the maximum accessible angles imposed by the finite numerical aperture of the used microscope lenses MO1 and MO2, the beams are slightly clipped, leading to an apparent decrease in transmission. This effect could obviously be reduced by staying away from these maximum angles. On the other hand, we want to investigate an as-large-as-possible number of independent illumination configurations (see above). Our choice of parameters is a trade-off between these two opposing conditions. Second, dirt and other imperfections on the involved optics also contribute to deviations from the expected unity transmission for all incident angles of light. These deviations are different for each incident direction of light. Third, fluctuations in laser power and the laser coherence length or vibrations of the setup during one experiment, which takes about 2 hours, also manifest as apparent transmission variations. While all of these three sources of deviations from unity transmission may appear as small effects in the experimental raw data at first

sight, the singular-value decomposition increases these unwanted variations in the resulting eigenvalue distributions.

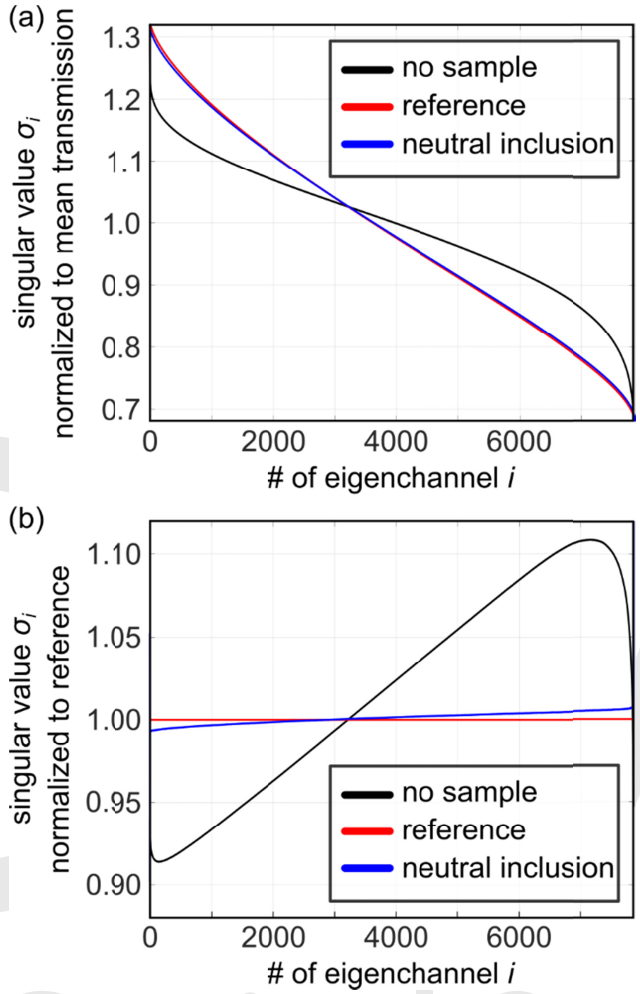

Fig. 5. (a) Modulus of the i-th singular value, $\sigma_i = |\sigma_{ii}|$, versus index $i = 1 \ldots 7{,}845$ for the case of no sample (black), the reference sample (red), and the core-shell neutral-inclusion sample (blue). (b) Same, but normalized to the singular value distribution of the homogeneously disordered reference sample.

Let us now come to considering samples in the setup. The decrease of the transmission eigenvalues versus index i in the no-sample case (black curve) is significantly less steep than the decrease for the core-shell neutral-inclusion sample (blue curve) or the reference sample (red curve) in Fig. 5(a). However, in this representation, one cannot see significant differences between the neutral-inclusion and the reference sample within the linewidth of the curves. Therefore, we normalize the data point-by-point with respect to one data set of the reference sample in Fig. 5(a). In this representation of the experimental data, the eigenvalue distributions of the neutral-inclusion and the reference sample are well separated.

To investigate whether this difference is reproducible and statistically significant, we have performed a number of additional experiments. In Fig. 6, we repeat each measurement on the reference sample and those on the core-shell neutral-inclusion sample several times each.

These measurements have intentionally been performed on different days and hence with individual alignments of the setup. Clearly, the difference in the eigenvalue distributions of reference and core-shell neutral-inclusion is reproducible.

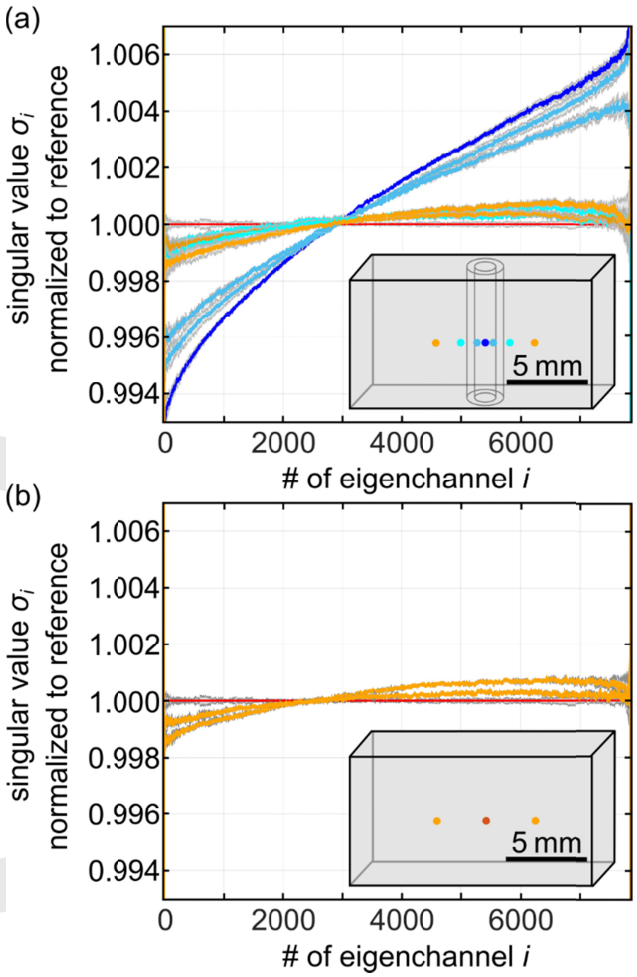

Fig. 6. (a) Same as Fig. 5(b), but for seven different positions on the core-shell neutral-inclusion sample (see inset). (b) Same as Fig. 5(b) but for three different positions (see inset) on the same reference sample. For each case, we show the average of five individual measurements by the full curve and the error bar (plus/minus one standard deviation) by the gray area. Note that the differences between the curves in (a) are much larger than those in (b). This observation means that the transmission-matrix experiments can reveal the invisible core-shell neutral-inclusion sample.

Next, we repeat the measurements on the core-shell neutral-inclusion sample, but move the illumination region on the front side of the sample (as well as the light-collection region on the rear side of the sample) by the indicated distances (see inset in Fig. 6(a)). Clearly, with increasing separation from the middle of the structure, the difference in the transmission eigenvalue distributions between the neutral-inclusion and the reference sample disappears – as one might have expected intuitively. More precisely, the magnitude of the transmission eigenvalues at small eigenchannel numbers i towards $i = 1$ gradually increase upon moving the illumination spot from the center (blue) of the structure towards the diffusive surrounding (orange). Far away from the center (orange), the behavior approaches that of the homogeneously disordered reference sample. In Fig. 6(b), different positions of the

illumination spot on the reference are depicted. As expected, no significant differences are observed. The observed difference in the maximum normalized transmission eigenvalue between the blue and orange curves agrees well with our previous time-of-flight experiments [12] discussed in the introduction: When illuminating the center (blue), the number of light scattering events is smaller due to the tendency of photons traveling through the shell, which has a larger diffusivity $D_2 > D_0$than the surrounding, D_0. Therefore, long-range correlations of multiply scattered waves, which determine the maximum normalized transmission eigenvalue, are weaker compared to illuminating the periphery of the neutral inclusion (orange). Going back to Fig. 5(a), the maximum normalized transmission eigenvalue is connected to the range or variance of the singular values spanned by the indices $i = 1 \ldots 7{,}845$. A reduced variance is again consistent with a reduction in wave correlation [22]. Therefore, we interpret the measured differences in the eigenvalue distributions of the neutral inclusion and the reference sample (or the surrounding of the neutral inclusion) as being due to differences in the wave correlation between these samples.

7. Conclusions

In conclusion, we have determined the optical transmission matrix of an invisible diffusive-optical core-shell neutral-inclusion and a homogeneously disordered reference sample by using interferometric experiments. From these transmission-matrix experiments, by using singular-value decomposition, we have extracted the transmission eigenvalues and eigenmodes. Due to the used normalization, the individual transmission eigenvalue distributions are independent of the mean transmissions of the sample. We find that the invisible diffusive neutral inclusion can be distinguished significantly from the diffusive reference sample along these lines.

However, while being statistically significant, these differences are rather small. In fact, it would have been much easier to distinguish the neutral-inclusion sample from the reference sample by inspection of the photographs of the samples shown in Fig. 1. Therefore, the notable message of our work is really that the neutral inclusion (or more generally the cloak), the design of which is solely based on the diffusion equation of light – which completely ignores the wave properties of light –, works surprisingly well on the level of light waves, too.

We hope that our experimental study will stimulate future theoretical work on wave propagation in three-dimensional piecewise homogeneously disordered media – which is presently elusive. Corresponding numerical calculations are presently demanding, but might become possible due to rapid advances in computation power.

Funding. This research has been funded by the Deutsche Forschungsgemeinschaft (DFG, German Research Foundation) through the priority program DFG-SPP 1839 “Tailored Disorder” and by the Karlsruhe School of Optics & Photonics (KSOP) and the Institute for Basic Science (IBS-R023-D1).

Acknowledgments. We thank Johann Westhauser (KIT) for technical support, and Ye-Ryoung Lee and Mooseok Jang for helpful discussion.

Disclosures. The authors declare no conflicts of interest.

Data availability. Data underlying the results presented in this paper are not publicly available at this time but may be obtained from the authors upon reasonable request.

References

1. C. M. Soukoulis, *Photonic Crystals and Light Localization in the 21st Century*, 1st ed. (Springer Science & Business Media, 2001).
2. C. M. Soukoulis and M. Wegener, "Past achievements and future challenges in the development of three-dimensional photonic metamaterials," Nat. Photonics **5**, 523–530 (2011).

3. R. Schittny, M. Kadic, T. Bückmann, and M. Wegener, "Invisibility cloaking in a diffusive light scattering medium," Science **345**, 427–429 (2014).
4. F. Gömöry, M. Solovyov, J. Šouc, C. Navau, J. Prat-Camps, and A. Sanchez, "Experimental Realization of a Magnetic Cloak," Science **335**, 1466–1468 (2012).
5. R. Schittny, M. Kadic, S. Guenneau, and M. Wegener, "Experiments on Transformation Thermodynamics: Molding the Flow of Heat," Phys. Rev. Lett. **110**, 195901 (2013).
6. E. H. Kerner, "The Electrical Conductivity of Composite Media," Proc. Phys. Soc. B **69**, 802 (1956).
7. G. W. Milton, *The Theory of Composites*, 1st ed. (Cambridge University Press, 2002).
8. R. Schittny, A. Niemeyer, F. Mayer, A. Naber, M. Kadic, and M. Wegener, "Invisibility cloaking in light scattering media," Laser Photonics Rev. **10**, 382–408 (2016).
9. F. Martelli, S. D. Bianco, A. Ismaelli, and G. Zaccanti, *Light Propagation Through Biological Tissue and Other Diffusive Media: Theory, Solutions, and Software*, 1st ed. (SPIE Press, 2010).
10. M. Kadic, T. Bückmann, R. Schittny, and M. Wegener, "Metamaterials beyond electromagnetism," Rep. Prog. Phys. **76**, 126501 (2013).
11. S. Mannherz, A. Niemeyer, F. Mayer, C. Kern, and M. Wegener, "On the limits of laminates in diffusive optics," Opt. Express **26**, 34274–34287 (2018).
12. R. Schittny, A. Niemeyer, M. Kadic, T. Bückmann, A. Naber, and M. Wegener, "Transient behavior of invisibility cloaks for diffusive light propagation," Optica **2**, 84–87 (2015).
13. A. Niemeyer, F. Mayer, A. Naber, M. Koirala, A. Yamilov, and M. Wegener, "Uncloaking diffusive-light invisibility cloaks by speckle analysis," Opt. Lett. **42**, 1998–2001 (2017).
14. S. M. Popoff, G. Lerosey, R. Carminati, M. Fink, A. C. Boccara, and S. Gigan, "Measuring the Transmission Matrix in Optics: An Approach to the Study and Control of Light Propagation in Disordered Media," Phys. Rev. Lett. **104**, 100601 (2010).
15. S. M. Popoff, G. Lerosey, M. Fink, A. C. Boccara, and S. Gigan, "Controlling light through optical disordered media: transmission matrix approach," New J. Phys. **13**, 123021 (2011).
16. W. Choi, A. P. Mosk, Q.-H. Park, and W. Choi, "Transmission eigenchannels in a disordered medium," Phys. Rev. B **83**, 134207 (2011).
17. M. Kim, W. Choi, Y. Choi, C. Yoon, and W. Choi, "Transmission matrix of a scattering medium and its applications in biophotonics," Opt. Express **23**, 12648–12668 (2015).
18. H. Yu, T. R. Hillman, W. Choi, J. O. Lee, M. S. Feld, R. R. Dasari, and Y. Park, "Measuring Large Optical Transmission Matrices of Disordered Media," Phys. Rev. Lett. **111**, 153902 (2013).
19. A. Goetschy and A. D. Stone, "Filtering Random Matrices: The Effect of Incomplete Channel Control in Multiple Scattering," Phys. Rev. Lett. **111**, 063901 (2013).
20. Y. Xu, H. Zhang, Y. Lin, and H. Zhu, "Light transmission properties in inhomogeneously-disordered random media," Ann. Phys. **529**, 1600225 (2017).
21. E. Akkermans and G. Montambaux, *Mesoscopic Physics of Electrons and Photons*, 1st ed. (Cambridge University Press, 2007).
22. C. W. Hsu, S. F. Liew, A. Goetschy, H. Cao, and A. Douglas Stone, "Correlation-enhanced control of wave focusing in disordered media," Nature Physics **13**, 497–502 (2017).
23. R. Schittny, A. Niemeyer, M. Kadic, T. Bückmann, A. Naber, and M. Wegener, "Diffuse-light all-solid-state invisibility cloak," Opt. Lett. **40**, 4202–4205 (2015).
24. L. Devaud, B. Rauer, J. Melchard, M. Kühmayer, S. Rotter, and S. Gigan, "Speckle engineering through singular value decomposition of the transmission matrix," arXiv:2010.06868 (2020).